Universidad Autónoma de Sinaloa
Facultad de Ciencias de la Tierra y el Espacio

Observatorio Infotecnológico
de las Ciencias de la Tierra y el Espacio

Boletín vol. 7, núm. 4
Diciembre 2019

UNIVERSIDAD AUTÓNOMA DE SINALOA
FACULTAD DE CIENCIAS DE LA TIERRA Y EL ESPACIO

Boletín Vol. 7, Núm. 4
Diciembre 2019

Contenido

Directorio

Dr. Juan Eulogio Guerra Liera
Rector

M.C. Jesús Madueña Molina
Secretario General

Dr. Wenseslao Plata Rocha
Director

M.C. Aníbal Israel Arana Medina
Secretario Académico

M.C. Jazive Rebeca Sánchez Jacobo
Coordinadora del Observatorio Infotecnológico

UNIVERSIDAD AUTÓNOMA DE SINALOA
FACULTAD DE CIENCIAS DE LA TIERRA Y EL ESPACIO

ARTÍCULOS: GEODESIA, GEOMÁTICA Y ASTRONOMÍA

GPS measured static and kinematic offsets at near and far field of the 2011 Mw 9.0 Tohoku-Oki earthquake

Gautam, P., Sathyaseelan, R., Pappachen, J., Kumar, N., Biswas, A., Philip, G., Dabral, C, and Pal, S., *Geodesy and Geodynamics,* 10, 213-227

Abstract

The Mw 9.0 Tohoku-Oki earthquake that hit the mainland Japan on 11th March, 2011 had resulted a devastating Tsunami due to an active thrusting between the Pacific and the North American Plates. Static and kinematic offsets at the offshore epicentre of the Mw 9.0 event remain unanswered and being investigated along with their near and far field limiting distances from the epicentre. Accordingly, offset measurements from 60 continuously operating IGS and GEONET GNSS stations were radially classified from the epicentre and interpreted with analytical models to find their linear offset decay rates. Co- and post-seismic static positional anomaly offsets of sixty days show almost all near field stations had strong or appreciable eastward or south eastward static shifts. Near stations (<250 km) showed both kinematic and static offsets. GEONET station '0175' showed maximum resultant static offset of ~4.5 m, which diminishes approximately 1e2 cm at far sites like SMST and AIRA. Characteristic decay duration (0b0) of the mean kinematic co-seismic shift (0a0) of near field stations was 17.28s during earthquake hours with an EW component shift >1.5 m. Spatial models of projected N-S static and kinematic offsets show their asymmetrical distributions around the epicentre with maximum model offset of - 1.84 m displaced towards south at ~45 km north of the epicentre. The Tohoku-Oki earthquake produced a resultant kinematic offset of ~10.2 m towards East at its offshore epicentre; while the estimated near field static offset is ~9.82 m. However, both estimates are bigger than double the resultant offset measured value (~4.3 m) in the Japanese mainland using GPS. The difference in the kinematic and static near field offsets highlight that the near surface had elastic or in-elastic kinematic strain dissipation as against the lithospheric level viscoelastic static response, which resulted rapid kinematic strain release (1.12 cm/km) within the limiting radius of ~220 km from the Tohoku-Oki epicentre.
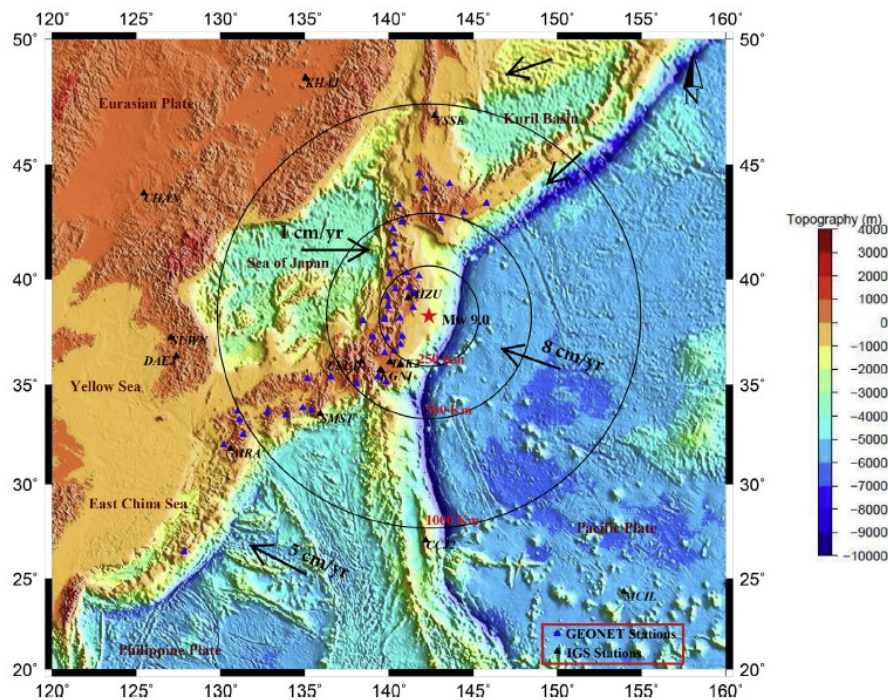
Figure 1. GEBCO bathymetry and topography of the study area with GPS sites from IGS and Japanese GEONET networks. The red star represents the epicentre of Mw9.0 Tohoku-Oki earthquake on11th March, 2011 at central Japan. The concentric circles represent various radial distances defined from the epicentre.

UNIVERSIDAD AUTÓNOMA DE SINALOA
FACULTAD DE CIENCIAS DE LA TIERRA Y EL ESPACIO

Lithosphere structures dynamics in the central High Atlas (Morocco) by seismic tomography and gravimetric data

Timoulali, Y., Bouiflane, M., Bouskri, G., Azguet, R., and El Fellah, Y., (2019). *Geodesy and Geodynamics,* 10, 241-255.

Abstract

We investigate sedimentological and tectonic processes at the central High Atlas, in order to understand their functioning and to build a geodynamic model that placed the area in its current geological frame.

The analysis used here is based on the numerical enhancement of a Landsat image where the main goal is to map surface sedimentary deposits throughout the central High Atlas in order to delimit the large geological structures. The sediment distribution throughout central High Atlas indicates that this one is a large tectonic subsiding basin, where the ongoing tectonic events and the geodynamical evolution remain to be explained by other prospecting techniques.

3-D structure velocities obtained by local seismic tomography and enhancement techniques of gravimetric anomalies are used to explore and define deep structure beneath the central High Atlas. The goal is to establish the evolution of the deep structure related to the geodynamical processes. Modest crustal thickness variation beneath the central High Atlas (~20e~40 km) define by local tomography and gravimetric anomalies, confirms that, a major part of the lower crust is detached into the lithosphere by delamination. Gravimetric anomaly, local seismic tomography and vertical cross sections throughout the central High Atlas, suggest that the lower crust detached is related to the broken slab of remain northward subduction beneath High and Middle Atlas. Meanwhile, extrusions of heated Asthenosphere materials induce the rifting stage concomitant to tectonic subsidence of the basin.
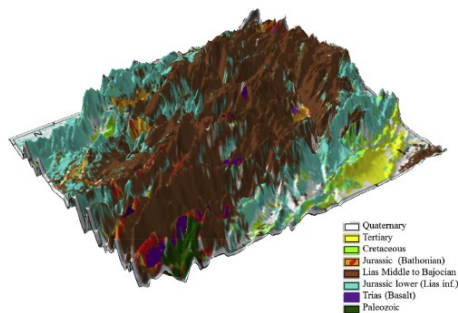

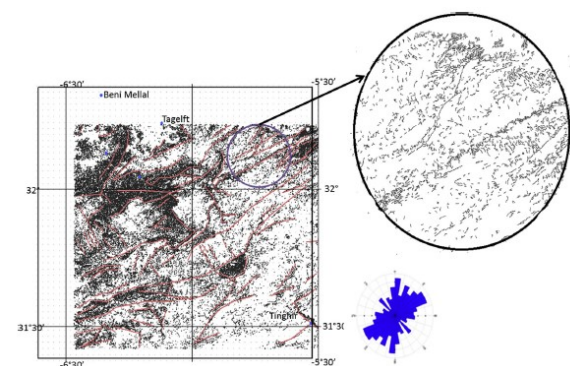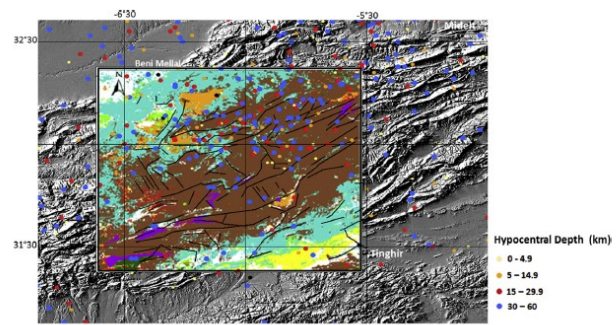**Figure 1.** The geological map overlain on the SRTM digital

Figure 2. Extraction and mapping the geological lineament. Polar diagram show the preferential direction NE-SW to NNE-SSW and the Minor directions WNW-ESE to NW-SE.
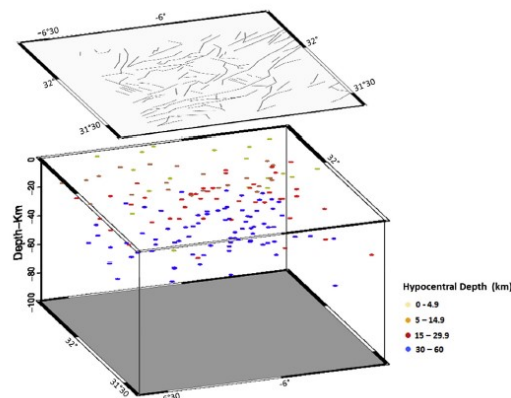

Figure 3. Intermediate depth seismicity (>40 km) activity is higher in the north-east of central High Atlas. The local seismic activity shows seismic axes superposed with some mapped.

UNIVERSIDAD AUTÓNOMA DE SINALOA
FACULTAD DE CIENCIAS DE LA TIERRA Y EL ESPACIO

# Co-seismic change in ocean bottom topography: Implication to absolute global mean sea level change

Kearns, T., Wang, G., Turco, M., Welch, J., Tsibanos, V. and Liu, H., (2018). *Geodesy and Geodynamics,* 10, 382-393.

Abstract

Earthquakes perturb both the ocean bottom topography due to displacements of sea floor and the geoid due to mass redistribution, which induces the relative sea level (RSL) change. However, the relative global mean sea level (GMSL) change is zero in that sea water mass is conserved. But the absolute GMSL change is not zero because earthquakes displace total ocean mass with respect to the Earth's center of mass (CM) which remains unchanged after an earthquake. This displacement, i.e. the absolute GMSL change, may be detectable by altimetry since the satellites are orbiting around CM. In this paper, we proposed a method to estimate co-seismic absolute GMSL change caused by earthquakes based on the point dislocation theory for a spherically symmetric, non-rotating, elastic and isotropic (SNREI) Earth.

This change can be directly connected to the perturbation of ocean bottom topography. We first computed co-seismic displacements as well as the change in geo-potential and solved the sea level equation to validate the insignificance of the oceans' feedback, i.e. the loading effect due to RSL change, to co-seismic displacements. The results imply that the loading effect due to RSL change is negligible on displacements while is considerable on geoid. We then computed the absolute GMSL change caused by co-seismic vertical and horizontal displacements by making use of the integrated Green's function method. The numerical results show that a large earthquake may raise the absolute GMSL by magnitude of sub-millimeter and the recent three large events cause GMSL to rise about one millimeter, inwhich the contribution from horizontal displacement is non-negligible.
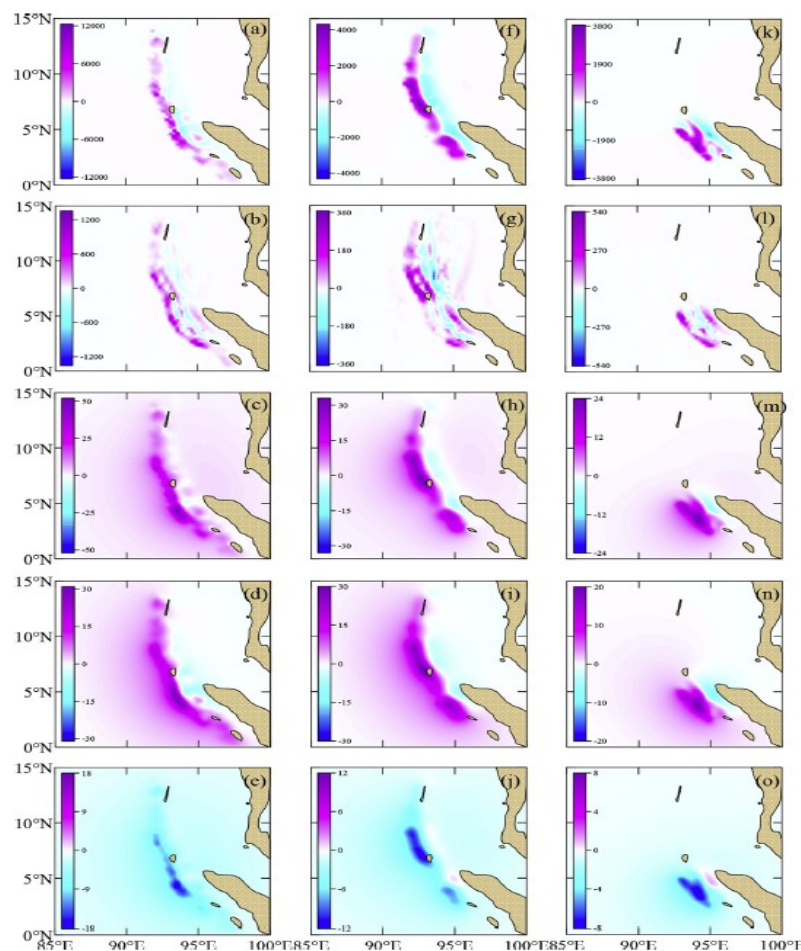
Figure 1. Water column height changes and geoid changes due to the 2004 Sumatra earthquake. (left, middle and right columns are for three different fault models, respectively. The five pictures from top to bottom are for the water column height changes due to co-seismic vertical displacement, horizontal displacement and loading, the co-seismic geoid change and the loading effect on geoid change, respectively. Unit in mm).

UNIVERSIDAD AUTÓNOMA DE SINALOA
FACULTAD DE CIENCIAS DE LA TIERRA Y EL ESPACIO

## SMOS brightness temperature forward modelling and long term monitoring at ECMWF

Abstract

This paper presents the forward modelling aspects of the SMOS (Soil Moisture and Ocean Salinity) activities at ECMWF (European Centre for Medium-Range Weather Forecasts). Several parameterizations of the Community Microwave Emission Modelling Platform (CMEM) are used to simulate L-band Brightness Temperatures (TBs) and compared to the SMOS TBs for 2010–2011. We show that simulated TBs are primarily sensitive, by order of importance, to the soil roughness model, the vegetation opacity and the soil dielectric model. In particular, best CMEM results are obtained with the simple Wigneron soil roughness model and the Wigneron model for the vegetation opacity. For the soil dielectric model, performances of the Wang and Schmugge and the Mironov models are shown to be similar and better than the Dobson model. The Wang and Schmugge model is then used in the next steps of this paper combined with the Wigneron roughness and vegetation models.

The paper describes a multi-angular multi-polarised bias correction method based on a linear rescaling (mean and variance) computed at the monthly scale using SMOS observations and ECMWF-CMEM re-analysed TBs for a four year period (2010–2013). Results show that for 2010–2013 the seasonal multi-angular multi-polarisation bias correction approach reduces global RMSE to 7.91 K, compared to 16.7 K before bias correction, whereas the mean absolute bias is reduced to 1.39 K, compared to 11.04 K before bias correction.

The consistency between the seasonality of simulated and the observed TBs is also improved by using a monthly bias correction, leading to correlation values improvement to 0.62 after bias correction compared to 0.56 before. The 2010–2013 bias correction applied to the 2014–2016 period at 40° incidence reduces the global RMSE from 15.56 K to 8.19 K, and the mean absolute bias from 10.16 K to 2.51 K, with no impact on the correlation values that remain at 0.61 in both cases. Long term monitoring of SMOS TB is presented covering a 7-year period (2010–2016) at both polarisations, at 40° incidence angle. Results show that the consistency between SMOS and ECMWF reanalysisbased TBs progressively improved between 2010 and 2016, pointing out improvements of level 1 SMOS TBproducts quality through the SMOS lifetime.
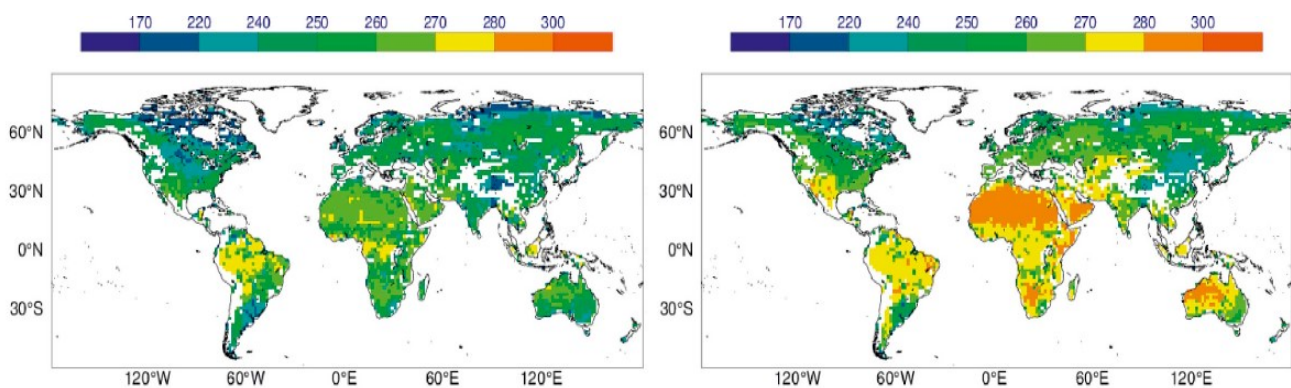
Figure 1. L-band TB (K) annual mean maps (2010–2011), at 40° incidence angle, X polarisation (left) and Y polarisation (right), observed by SMOS (a), simulated by ECMWF (

UNIVERSIDAD AUTÓNOMA DE SINALOA
FACULTAD DE CIENCIAS DE LA TIERRA Y EL ESPACIO

Drainage basin delineation for outlet glaciers of Northeast Greenland based on Sentinel-1 ice velocities and TanDEM-X elevations

Krieger, L., Floriciuiu, D. and Neckel, N., (2020). *Remote Sensing of Enviromental.* 237.

Abstract

The drainage divides of ice sheets separate the overall glaciated area into multiple sectors. These drainage basins are essential for partitioning mass changes of the ice sheet, as they specify the area over which basin specific measurements are integrated. The delineation of drainage basins on ice sheets is challenging due to their gentle slopes accompanied by local terrain disturbances and complex patterns of ice movement. Until now, in Greenland the basins have been mostly delineated along the major ice divides, which results in large drainage sectors containing multiple outlet glaciers. However, when focusing on measuring glaciological parameters of individual outlet glaciers, more detailed drainage basin delineations are needed. Here we present for the first time a detailed and fully traceable approach that combines ice sheet wide velocity measurements by Sentinel-1 and the high resolution TanDEM-X global DEM to derive individual glacier drainage basins. We delineated catchments for the Northeast Greenland Ice Sheet with a modified watershed algorithm and present results for 31 drainage basins. Even though validation of drainage basins remains a difficult task, we estimated basin probabilities from Monte-Carlo experiments and applied the method to a variety of different ice velocity and DEM datasets finding discrepancies of up to 16% in the extent of catchment areas. The proposed approach has the potential to produce drainage areas for the entirety of the Greenland and Antarctic ice sheets.
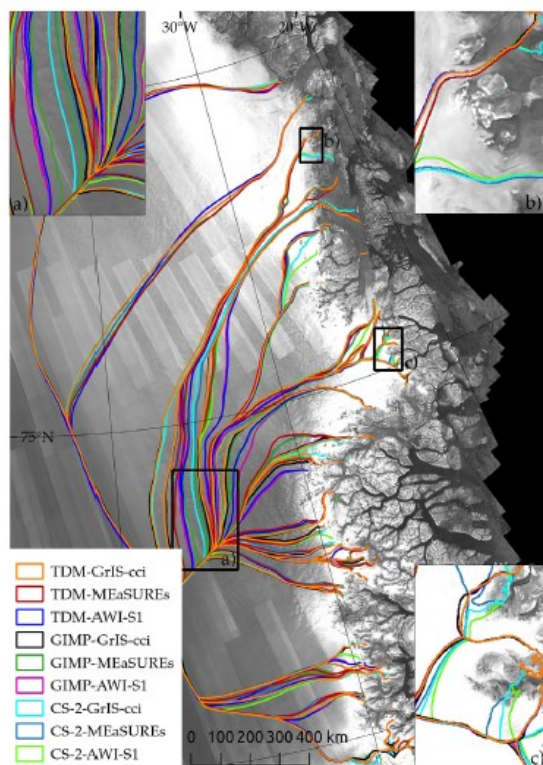
Figure 1. The basin boundaries resulting from all input DEM and velocity dataset combinations. Inset (a): different delineations that originate from diverging ice flow directions at lower elevations. (b) and (c): places where CS-2 delineations are at different locations than the GIMP and TDM based boundaries. In the background the TDM SAR backscattering amplitude mosaic.
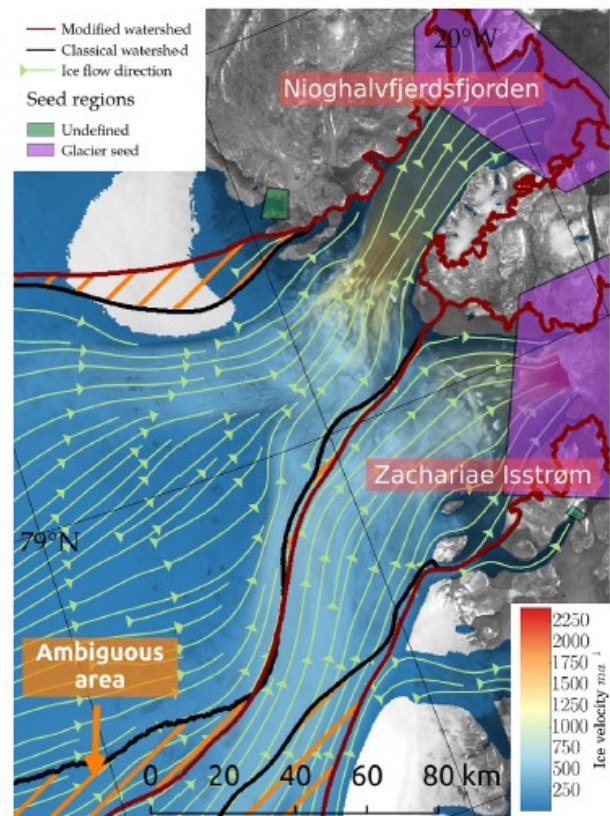
Figure 2. Watershed lines separating the two glaciers 79North and Zachariæ Isstrøm derived by the classical watershed algorithm based solely on DEM information (black line) compared to the basin boundary when additional ice velocity is used (red line). The disagreement between the drainage divides leads to an ambiguous area which according to the ice flow direction (green arrows) is misclassified by the classical watershed procedure. In the background the TDM SAR backscattering amplitude mosaic.

UNIVERSIDAD AUTÓNOMA DE SINALOA
FACULTAD DE CIENCIAS DE LA TIERRA Y EL ESPACIO

## Automated water surface temperature retrieval from Landsat 8/TIRS

Abstract

Satellite remote sensing of Land and Water Surface Temperature (L/WST) has many applications in studies of terrestrial and aquatic ecology. Retrieval of L/WST requires a well calibrated radiometer and an accurate atmospheric correction. In the present study, the performance of the Thermal InfraRed Sensor (TIRS) on board Landsat 8 is evaluated for the retrieval of L/WST. LibRadtran is used to retrieve atmospheric correction parameters based on atmospheric profiles of relative humidity and temperature from three global atmospheric models. Performance of single band retrievals is compared to typical MODTRAN results from the Atmospheric Correction Parameter Calculator (ACPC) and a split-window approach. A multi-temporal land masking methodusing imagery from the Operational Land Imager (OLI) on board Landsat 8 is demonstrated, and is used to automatically classify imagery in the matchup dataset in three classes of cloud cover.

Two sources of in situ data covering the Belgian Coastal Zone (BCZ) are used for validation of the L/WST product: (1) fixed locations in the Flemish Banks measurement network and (2) underway data from regular RV Belgica campaigns. In the present study the single band methods outperformed the split-window approach, and consistent retrievals are found for the MODTRAN and libRadtran simulations. Typical single band surface temperature retrievals in quasi cloudfree conditions have Root Mean Squared Differences (RMSD) of 0.7 K and 1 K for Bands 10 and 11 with low bias, depending on the method and atmospheric profile source. For imagery with scattered clouds, RMSD values increase to 1 K and 2 K respectively with an approximately 0.5 K cold bias, likely caused by cloud proximity.

The calibration efforts combined into Collection 1 allows for accurate absolute surface temperature retrievals from B10 on Landsat 8/TIRS for homogeneous targets with known emissivity, such as liquid water. The method is adapted to global processing and can be used for Land Surface Temperature retrieval with a suitable source of emissivity data.
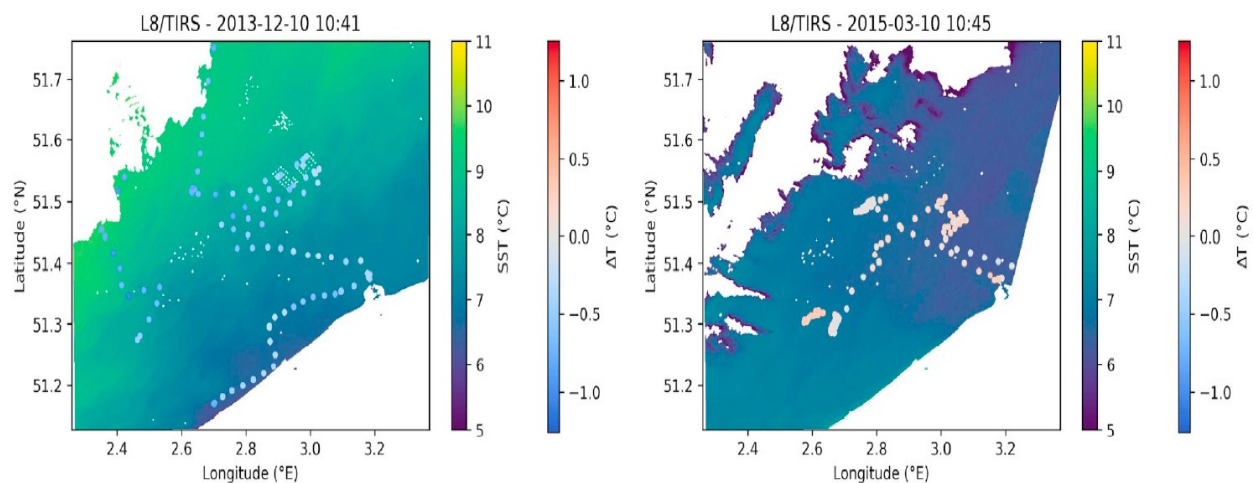
Figure 1. Two of the more complete tracks of Belgica/ODAS underway data and L8/TIRS temperature, with temperature difference (T=satellite-in situ) plotted at the sampling locations. White areas denote missing data due to non-water masking and swath edge. Note the undetected thin clouds (cold areas) on the 2015-03-10 image.

UNIVERSIDAD AUTÓNOMA DE SINALOA
FACULTAD DE CIENCIAS DE LA TIERRA Y EL ESPACIO

The TORUS radiation transfer code

Harris, T., Haworth, T., Acreman, D., Ali, A., Douglas, (2019). *Astronomy and Computing ,* 27, 63-95.

Abstract

We present a review of the torus radiation transfer and hydrodynamics code. torus uses a 1-D, 2-D or 3-D adaptive mesh refinement scheme to store and manipulate the state variables, and solves the equation of radiative transfer using Monte Carlo techniques. A framework of microphysics modules is described, including atomic and molecular line transport in moving media, dust radiative equilibrium, photoionisation equilibrium, and time-dependent radiative transfer. These modules provide a flexible scheme for producing synthetic observations, either from analytical models or as post-processing of hydrodynamical simulations (both grid-based and Lagrangian). A hydrodynamics module is also presented, which may be used in combination with the radiation-transport modules to perform radiation-hydrodynamics simulations. Benchmarking and validation tests of each major mode of operation are detailed, along with descriptions and performance/scaling tests of the various parallelisation schemes. We give examples on the uses of the code in the literature, including applications to lowand high-mass star formation, cluster feedback, and stellar winds, along with an Appendix listing the refereed papers that have used torus.
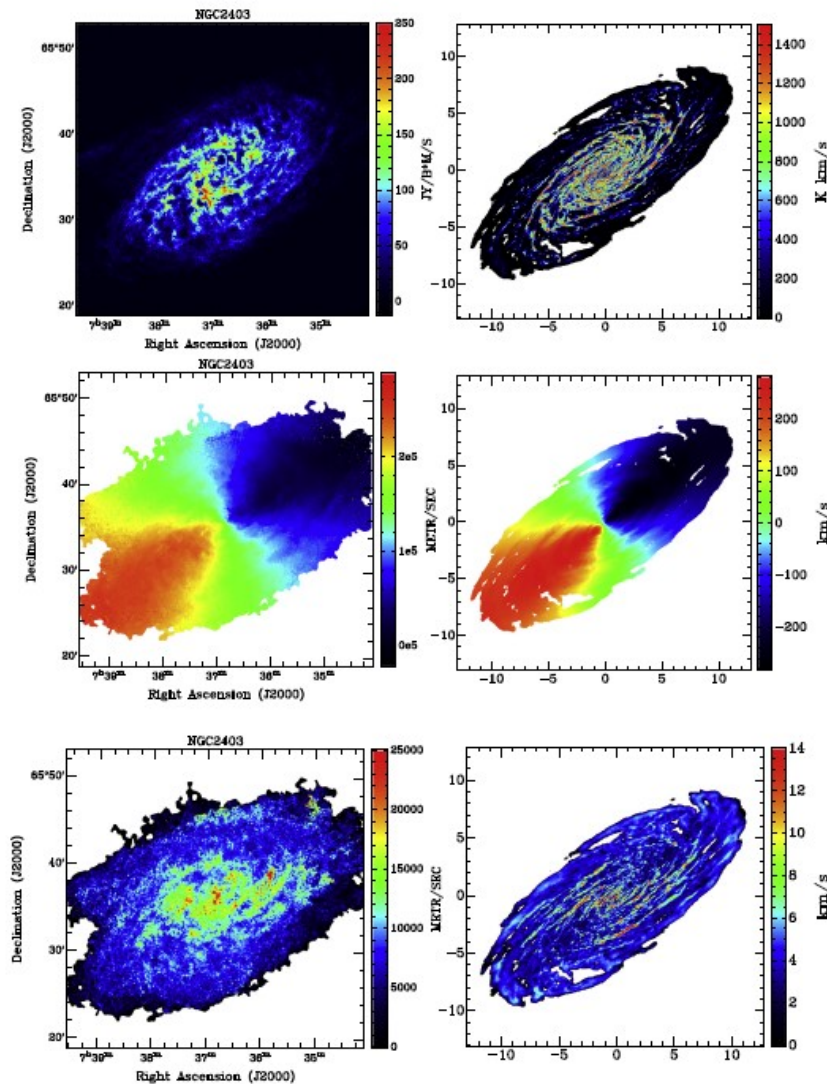
Figure 1. Hi moment maps from observations (left) and a torus model (right). The zero moment (top row) is the integrated intensity, the first moment (middle row) is the emission weighted velocity, and the second moment (bottom row) measures the velocity dispersion. The observations are NGC2403 from the THINGS survey (Walter et al., 2008). The axes on the plots are in units of kpc.

UNIVERSIDAD AUTÓNOMA DE SINALOA
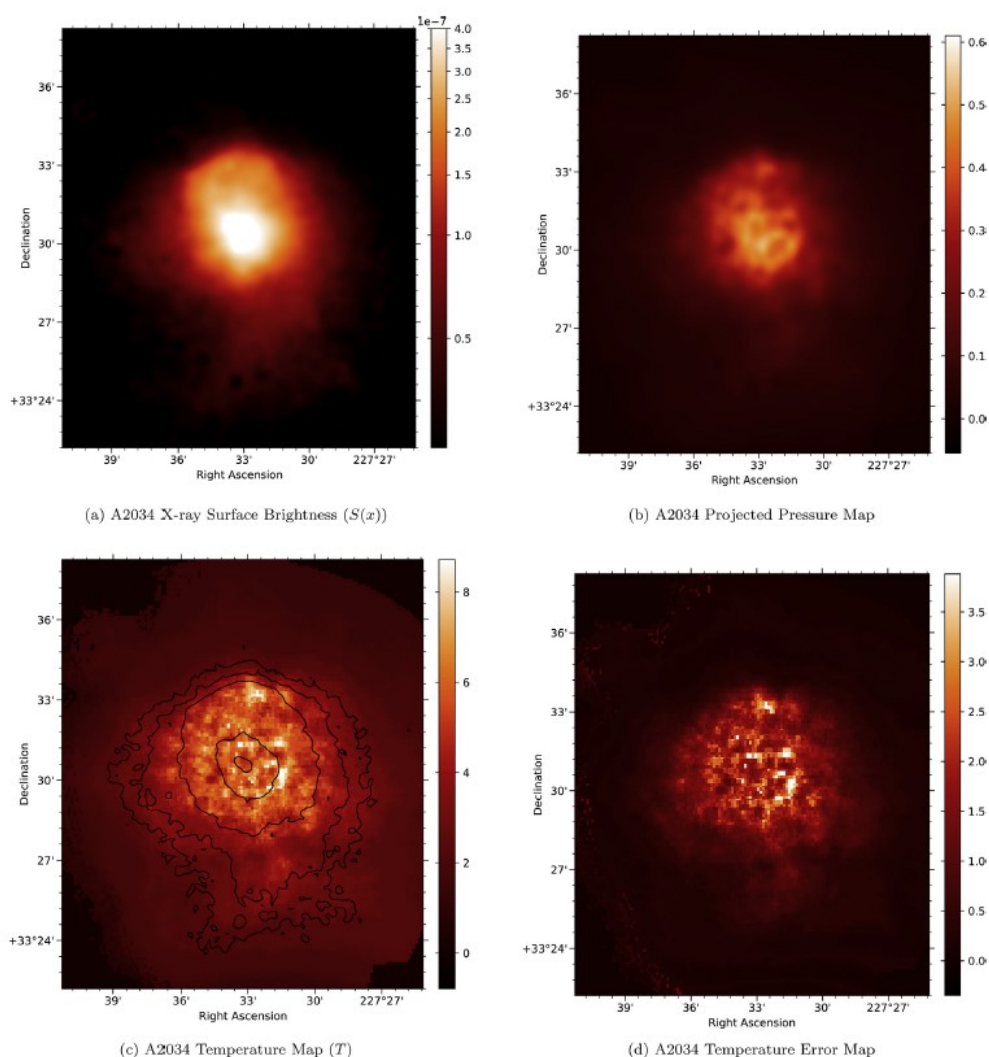FACULTAD DE CIENCIAS DE LA TIERRA Y EL ESPACIO

The galaxy cluster 'Pypeline' for X-ray temperature maps: ClusterPyXT

Alden, B., Hallman, E., Rapetti, D., Burns, J. and Datta. A. , (2019). *Astronomy and Computing* , 27, 147-155.

Abstract

ClusterPyXT is a new software pipeline to generate spectral temperature, X-ray surface brightness, pressure, and density maps from X-ray observations of galaxy clusters. These data products help to elucidate the physics of processes occurring within clusters of galaxies, including turbulence, shock fronts, nonthermal phenomena, and the overall dynamics of cluster mergers. ClusterPyXT automates the creation of these data products with minimal user interaction, and allows for rapid analyses of archival data with user defined parameters and the ability to straightforwardly incorporate additional observations. In this paper, we describe in detail the use of this code and release it as an open Source Python project on GitHub.

(a) A2034 X-ray Surface Brightness ($S(x)$)

(b) A2034 Projected Pressure Map

(c) A2034 Temperature Map (T)

(d) A2034 Temperature Error Map

Figure 1. Top left: X-ray surface brightness map for A2034 (in counts/cm2/s). The image is smoothed using a Gaussian kernel of 2.5″ . The observation IDs used in this image are 7695, 2204, 12885, 13192, 12886, and 13193. Top right: Projected pseudo pressure map for A2034. This map is generated using the relation P = [S(x)](1/2)T . Bottom left: ACB temperature map for A2034 with X-ray surface brightness contours in black. The contour levels depicted are 4, 6, 13, 38, and 63 percent of peak emission (7.91 × 10−7 counts/cm2/s). Bottom right: Temperature error map for A2034 representing 1σ error bars for panel 6c.

UNIVERSIDAD AUTÓNOMA DE SINALOA
FACULTAD DE CIENCIAS DE LA TIERRA Y EL ESPACIO

NOTICIAS

Veinte años de XMM-Newton en el espacio

El 10 de diciembre, el observatorio espacial de rayos X XMM-Newton de la ESA cumplió 20 años. En estas dos décadas, no ha dejado en ningún momento de proporcionarnos ciencia de primer nivel. Un ámbito en el que la misión ha destacado especialmente ha sido el de los agujeros negros, haciendo que cambiemos radicalmente la forma de entender estos enigmas cósmico. Los agujeros negros son objetos celestes tan densos que ni siquiera la luz puede escapar de ellos. En esta representación artística, las extrañas formas de la luz que rodean el agujero negro representan lo que las simulaciones informáticas predicen que sucedería en las inmediaciones de su intenso campo gravitacional

Aunque, en realidad, ni XMM-Newton ni ningún otro telescopio puede ver agujeros negros con este nivel de detalle, los datos y las observaciones de la misión constituyen una importante fuente de información sobre estas misteriosas trampas gravitacionales.

Noticia completa en: https://noticiasdelaciencia.com/art/35763/veinte-anos-de-xmm-newton-en-el-espacio

Las estrellas de un sistema binario se acercan por la emisión de ondas gravitatorias
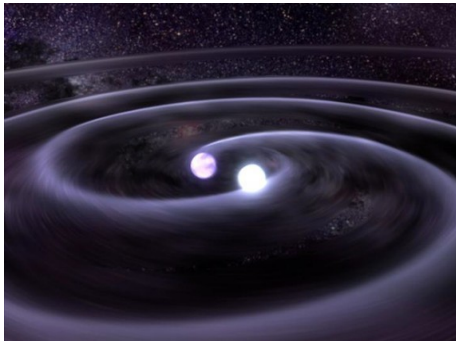
Cada 20 minutos, las estrellas del sistema doble PTF J053332.05+020911.6 completan una órbita en torno al centro de masas común, una frecuencia que apunta a que se trata de un sistema excepcional: no está formado por estrellas 'normales', sino por enanas blancas, y esa velocidad genera efectos de marea que deforman las estrellas, que presentan forma elipsoidal.

Un trabajo, en el que participa el Instituto de Astrofísica de Andalucía y publicado en The Astrophysical Journal Letters, se ha centrado en este sistema y ha hallado que las estrellas muestran un decaimiento orbital, que las acerca progresivamente, debido a la emisión de ondas gravitatorias. Las enanas blancas, como las que forman este sistema, constituyen los restos de una estrella como el Sol que ha expulsado sus capas más externas y conserva un núcleo muy compacto. Las densidades de estos objetos pueden ascender a dos toneladas por centímetro cúbico, y pueden albergar una masa equivalente a la del Sol en un volumen similar al de la Tierra.

Noticia completa en: https://noticiasdelaciencia.com/art/34972/miles-de-nuevos-cumulos-globulares-se-han-formado-en-los-ultimos-mil-millones-de-anos

El agua es común, aunque escasa, en los exoplanetas

La más amplia inspección de composiciones químicas atmosféricas de exoplanetas realizada hasta la fecha ha puesto de manifiesto tendencias que desafían las actuales teorías de la formación de planetas, y tiene implicaciones en la búsqueda de agua en el propio sistema solar y más allá.

Un equipo de científicos, liderado por la University of Cambridge, utilizó datos atmosféricos de 19 exoplanetas (planetas alrededor de otras estrellas) para obtener mediciones detalladas de sus propiedades químicas y térmicas. Los exoplanetas en el estudio tenían una amplia variedad de tamaños, desde "miniNeptunos" de casi 10 veces la masa de la Tierra hasta "superJúpiteres" de más de 600 masas terrestres, y con temperaturas que van de 20 a 2.000 grados C. Como los planetas gigantes de nuestro sistema solar, sus atmósferas son ricas en hidrógeno, pero orbitan tipos diferentes de estrellas.

Según Nikku Madhusudhan, jefe del programa, se están viendo los primeros signos de perfiles químicos en mundos extraterrestres, y puede apreciarse cuán diversos pueden ser en cuanto a sus composiciones químicas.

Noticia completa en: https://noticiasdelaciencia.com/art/35754/el-agua-es-comun-aunque-escasa-en-los-exoplanetas

UNIVERSIDAD AUTÓNOMA DE SINALOA
FACULTAD DE CIENCIAS DE LA TIERRA Y EL ESPACIO

CONGRESOS

XI Congreso Internacional Geomática 2020

Sede: La Habana, Cuba

Fecha: 16 al 20 de marzo del 2020

Más información en: http://www.nosolosig.com/geo-eventos/1093-xi-congreso-internacional-de-geomatica-2020

II Congreso Internacional del Desarrollo Territorial

Sede: Rafaela, Santa Fe, Argentina

Fecha: 7 y 8 de Octubre del 2020

Más información en: http://www.conectadel.org/wp-content/uploads/2019/12/I%C2%BA-Circular-II-Congreso-Internacional-Desarrollo-Territorial-RafaelaOctubre2020.pdf